Supporting Information for:

Suppressing argyrodite oxidation by tuning the host structure for high areal capacity all-solid-state lithium-sulfur batteries

*Zhuo Yu, Baltej Singh, Yue Yu, Linda F. Nazar**

Department of Chemistry and the Waterloo Institute for Nanotechnology, University of Waterloo, 200 University Avenue West, Waterloo, Ontario N2L 3G1, Canada

Corresponding Author
*E-mail: lfnazar@uwaterloo.ca

LIST OF SUPPLEMENTAL FIGURES

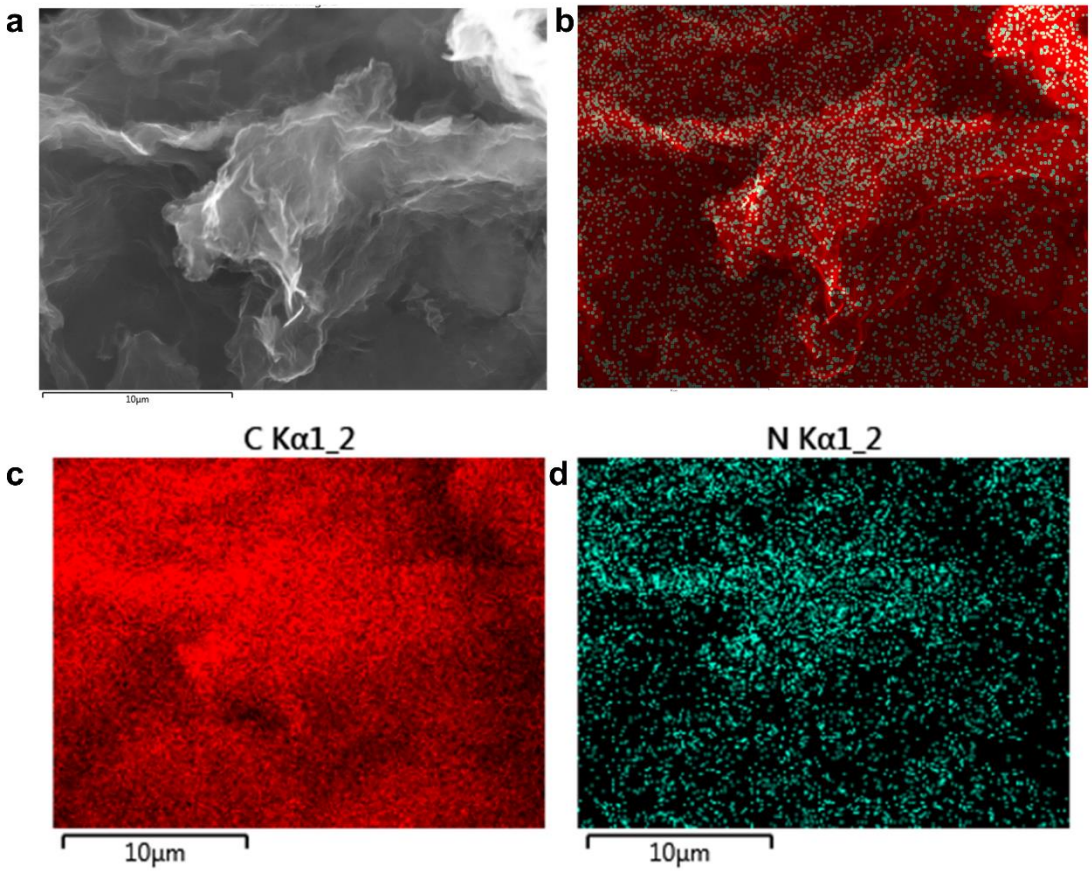

Supplementary Figure 1. a-d, SEM image of CNG (**a**) and its corresponding EDX elemental mapping, overall (**b**), C (**c**) and N (**d**) mapping are shown, respectively.

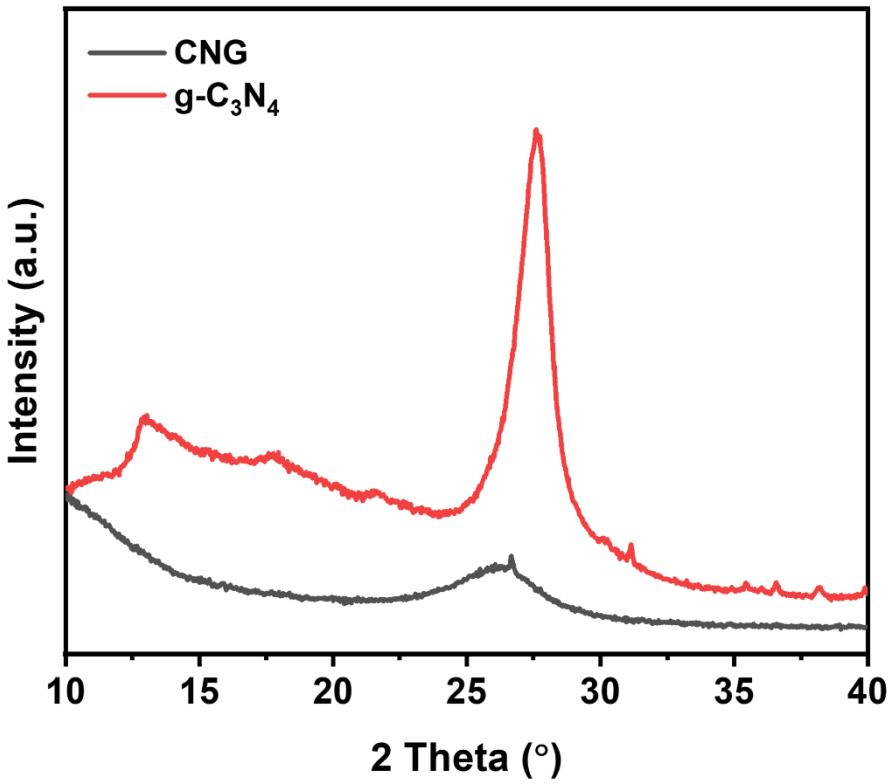

Supplementary Figure 2. XRD pattern of CNG and g-C_3N_4.

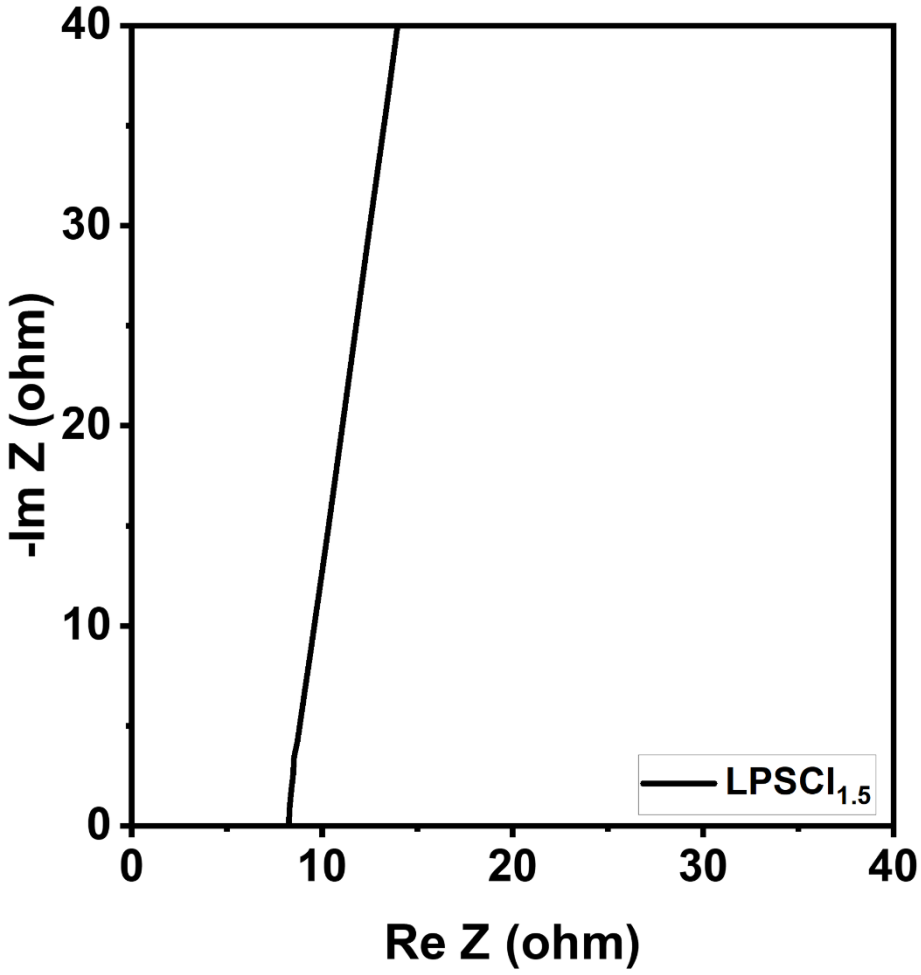

Supplementary Figure 3. Ionic conductivity of $LPSCl_{1.5}$ measured by EIS. The conductivity is calculated to be 10 mS cm^{-1}. The ionic conductivity was calculated using the equation, $\sigma = t/AR$ where σ is the ionic conductivity, t is the thickness of the SE pellet, A is the area of the SE pellet and R is the impedance from the Nyquist plot. Herein, σ ($LPSCl_{1.5}$) = 0.065 cm/ (0.785 cm^2 * 8.2 Ω) = 10 mS cm^{-1}.

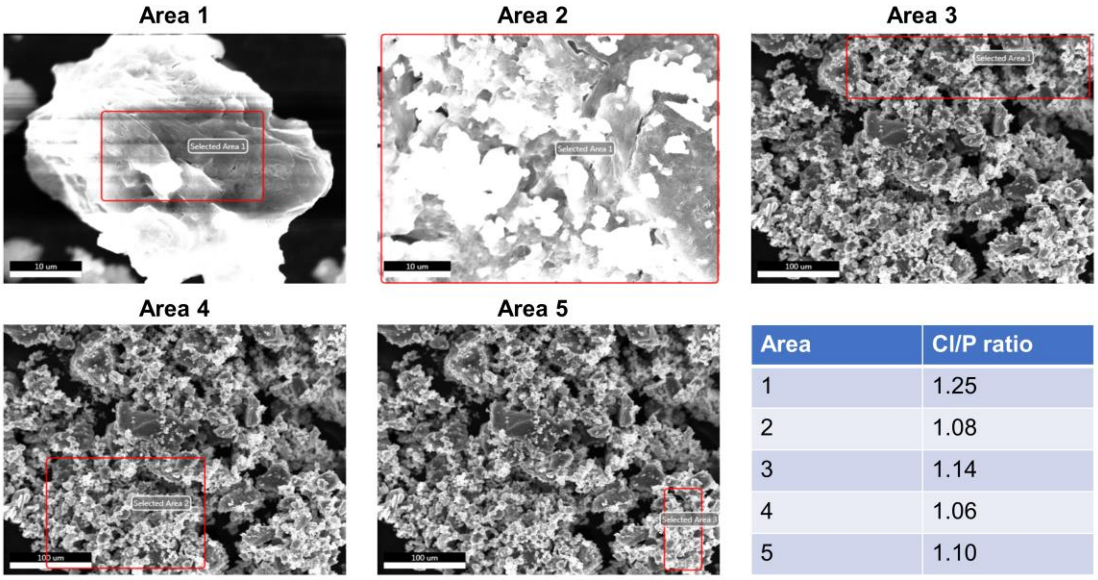

Area	Cl/P ratio
1	1.25
2	1.08
3	1.14
4	1.06
5	1.10

Supplementary Figure 4. SEM-EDX analysis of as-synthesized $LPSCl_{1.5}$. The figures show the five selected areas and the Cl/P ratios are summarized in the table.

Supplementary note 1. Calculation of theoretical oxidation capacity of argyrodites. According to the indirect degradation pathway,[1] the LPSC will first lose two lithium ions and form Li_4PS_5Cl,

$$Li_6PS_5Cl \rightarrow Li_4PS_5Cl^{2-} + 2Li^+$$

Li_4PS_5Cl rapidly decomposes,

$$Li_4PS_5Cl^{2-} \rightarrow Li_3PS_4 + LiCl + S + 2e^-$$

Above 2.9 V, Li_3PS_4 is oxidized to S,

$$Li_3PS_4 \rightarrow {}^1/_2\, P_2S_7^{4-} + {}^1/_2\, S + 3Li^+ + e^-$$

Based on the 3-electron oxidation process, the theoretical capacity of LPSC is 299.6 mAh g^{-1}.

Likewise, the theoretical capacity of $LPSCl_{1.5}$ is 201 mAh g^{-1}. Note that VC/$LPSCl_{1.5}$ cell showed a capacity of 277 mAh g^{-1} which exceeds the theoretical value of $LPSCl_{1.5}$.

We thus performed SEM-EDX analysis as shown in **Supplementary Figure 4**. Five areas were selected to ensure good statistics. The average Cl/P ratio is 1.1. Therefore, the as-synthesized $LPSCl_{1.5}$ was corrected to an actual stoichiometry of $LPSCl_{1.1}$ with a theoretical capacity of 280 mAh g^{-1}.

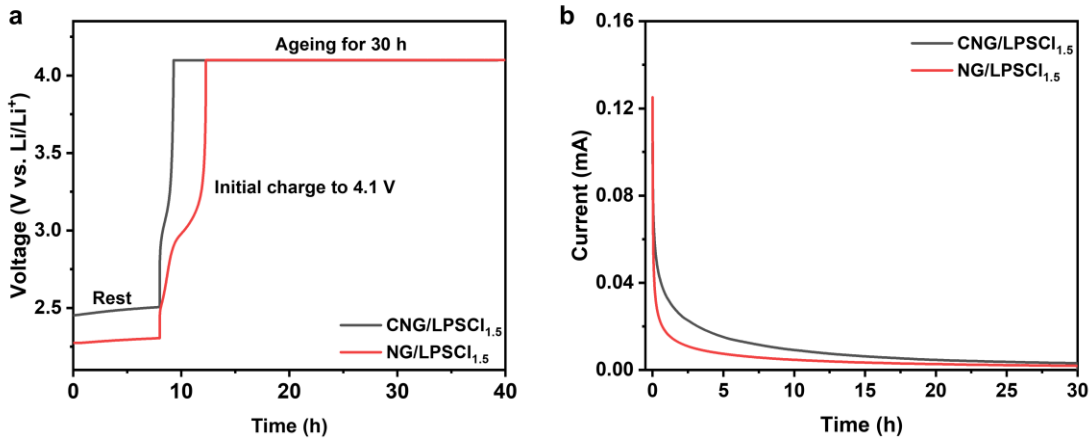

Supplementary Figure 5. Aging tests. **a**, Voltage-time profiles of aging tests for Li-In|$LPSCl_{1.5}$|CNG (or NG)/S/$LPSCl_{1.5}$ SSSBs. The cells were first rested for 8 hours, then charged to 4.1 V versus Li/Li^+ and aged for 30 hours. **b**, Leakage current during a hold for 30 h at a constant voltage of 4.1 V versus Li/Li^+ after initial charge.

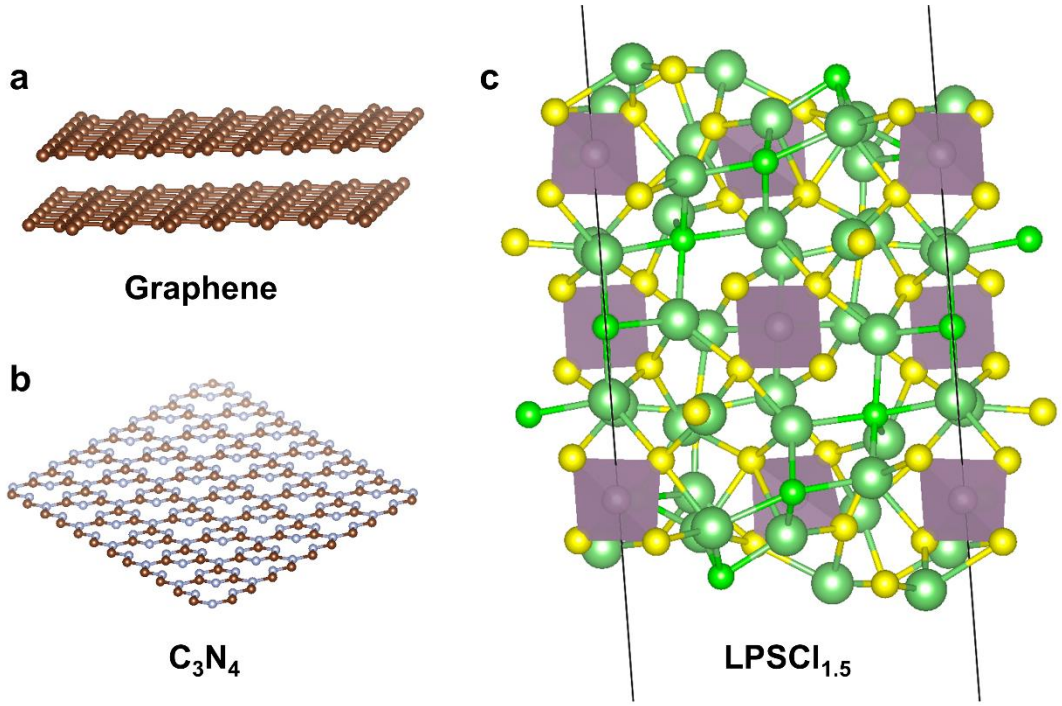

Supplementary Figure 6. DFT relaxed configuration of (**a**) bilayer graphene; (**b**) monolayer C_3N_4 and (**c**) $LPSCl_{1.5}$, (010) surface.

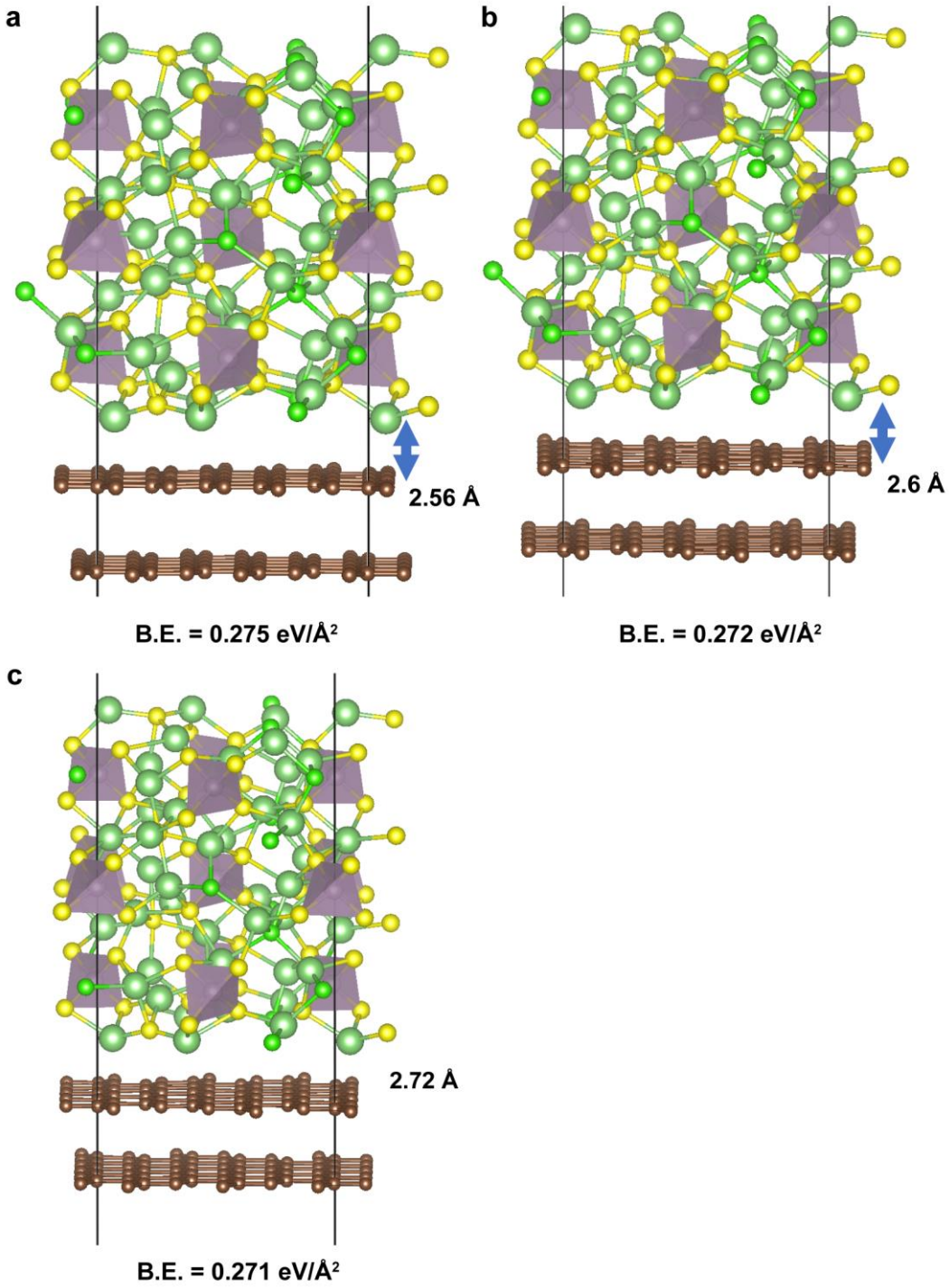

Supplementary Figure 7. a-c, DFT calculated binding energies for three different configurations, I (**a**), II (**b**), III (**c**) of $LPSCl_{1.5}$-graphene interfaces.

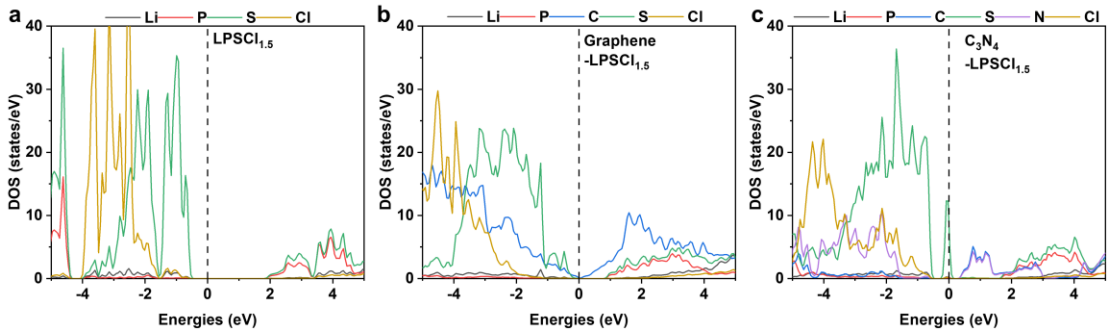

Supplementary Figure 8. PBE-DFT calculated DOS for pristine $LPSCl_{1.5}$ (**a**), graphene-$LPSCl_{1.5}$ (**b**) and C_3N_4-$LPSCl_{1.5}$ (**c**) composite configurations, respectively.

We used PBE-DFT calculations to calculate total and atom-projected electronic density of states (DOS) for $LPSCl_{1.5}$, graphene-$LPSCl_{1.5}$, and C_3N_4-LPSCl1.5 to understand and compare the electronic transport at the interfaces. While PBE-DFT tends to underestimate band gaps, we focused on comparison of atom-projected and total DOS at various interfaces. Specifically, the graphene-$LPSCl_{1.5}$ interface is enriched with Li, S, and C atoms, which significantly contribute to the valence and conduction band near the Fermi level, favoring electronic transport. Conversely, electronic conduction is less favorable at the C_3N_4-$LPSCl_{1.5}$ interface due to the absence of Li DOS because the interface relies on Li-N bonds, whereas the valence and conduction bands are mainly contributed by S atoms and C/N atoms respectively. A small DOS above the Fermi level arises from the smearing of the calculated DOS.

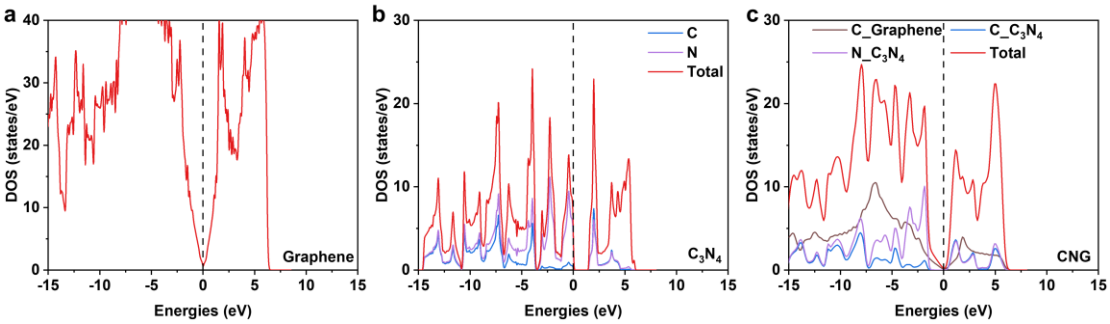

Supplementary Figure 9. DOS analysis of graphene (**a**), C_3N_4 (**b**), and CNG (**c**).

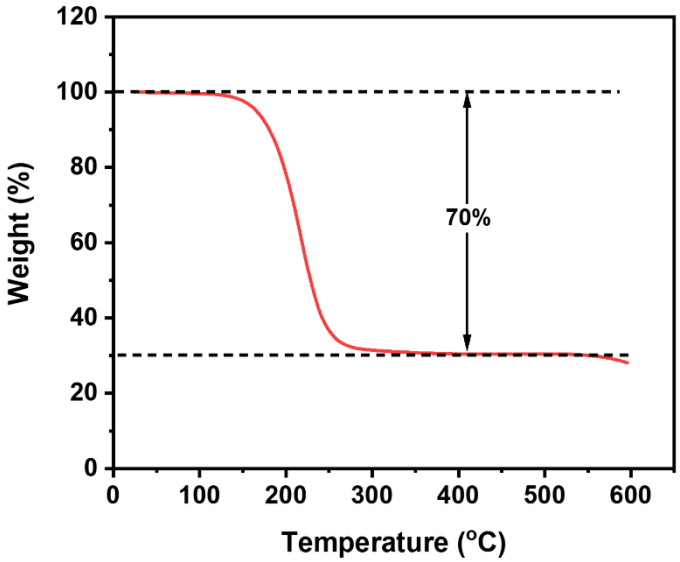

Supplementary Figure 10. TGA curve of CNG/S. The sulfur mass content was 70%.

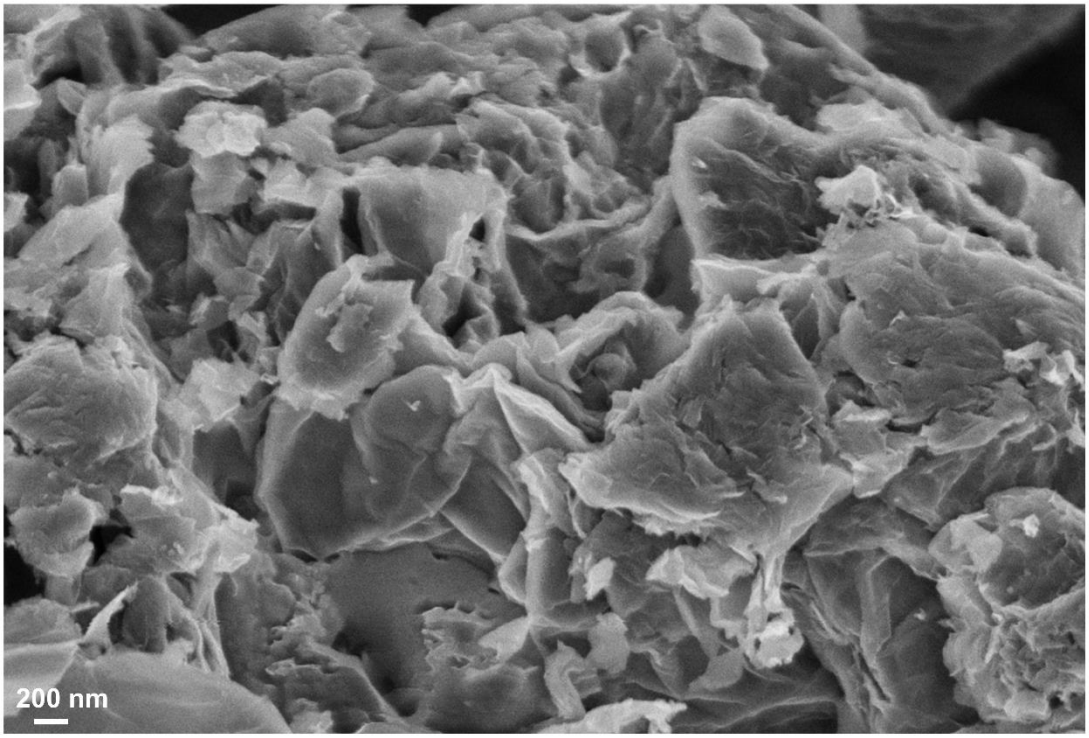

Supplementary Figure 11. SEM image of the CNG/S composite.

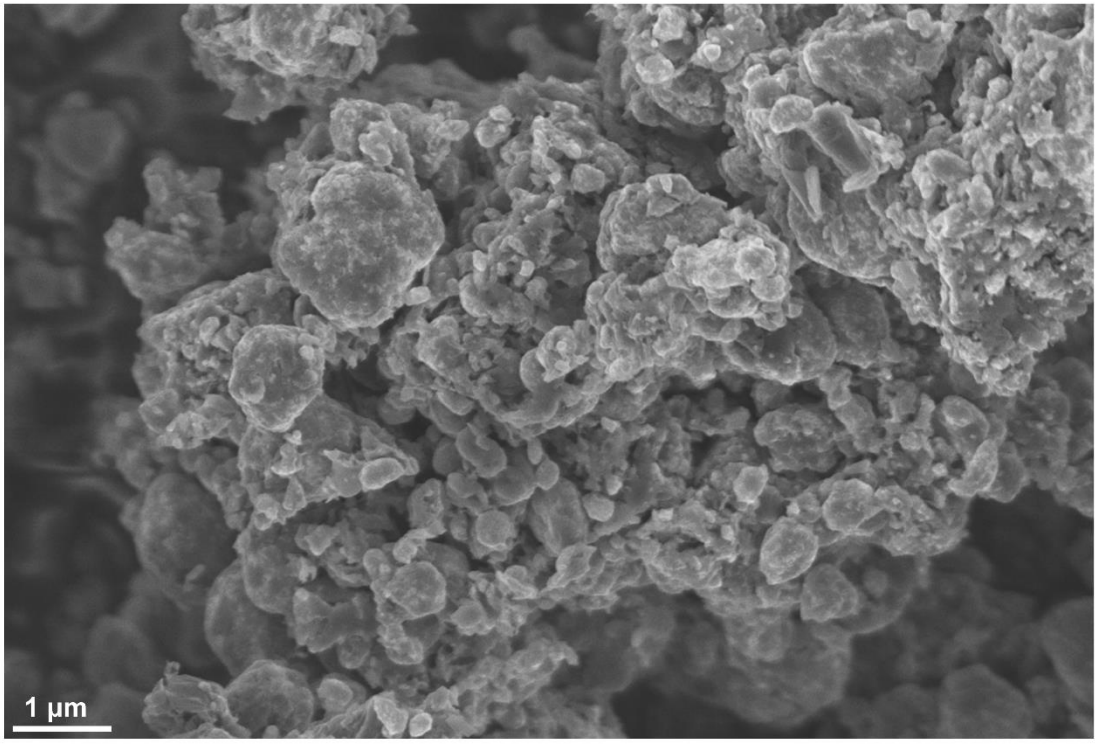

Supplementary Figure 12. SEM image of the CNG/S/LPSCl$_{1.5}$ cathode composite.

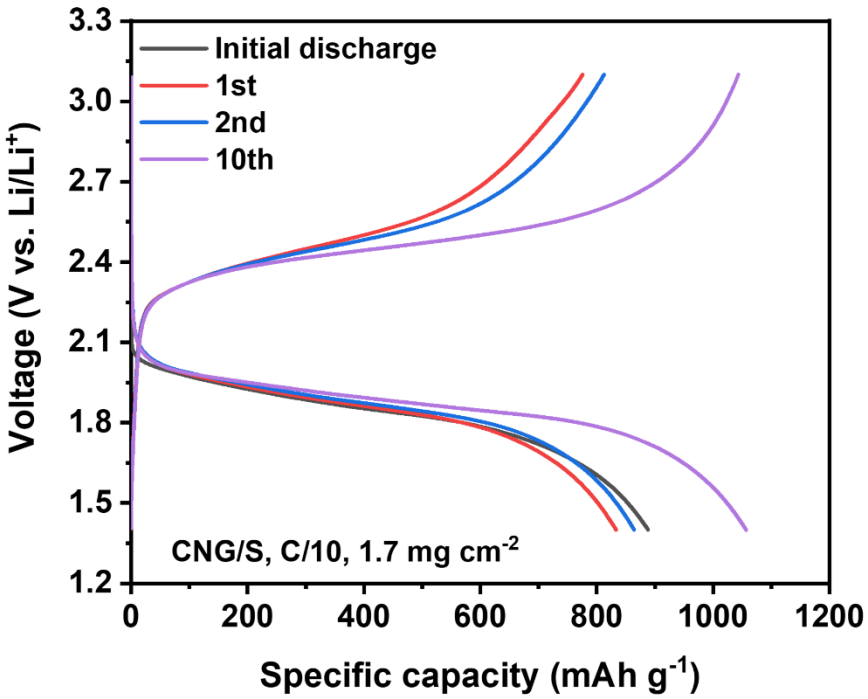

Supplementary Figure 13. Voltage profiles of Li-In|$LPSCl_{1.5}$|CNG/S/$LPSCl_{1.5}$ SSSB cycled at C/10 at room temperature.

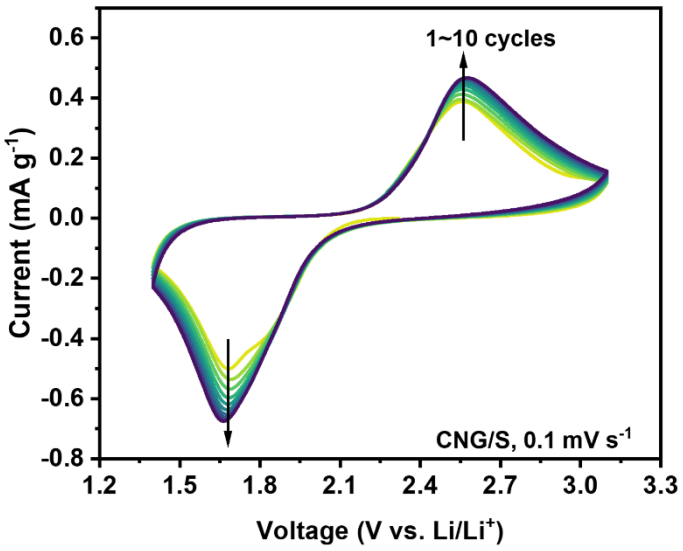

Supplementary Figure 14. CV curves of CNG/S SSSB at a scan rate of 0.1 mV s^{-1}.

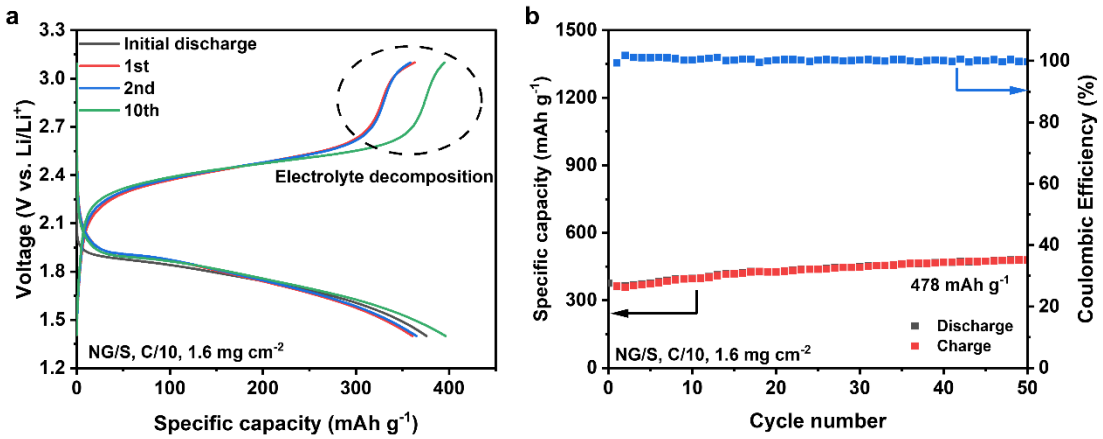

Supplementary Figure 15. Electrochemical performance of Li-In|LPSCl$_{1.5}$|NG/S/LPSCl$_{1.5}$ SSSB at room temperature. a, Voltage profiles at C/10 with a sulfur loading of 1.6 mg cm^{-2}. b, Corresponding cycling performance. The electrolyte decomposition can be clearly seen in the charge profile.

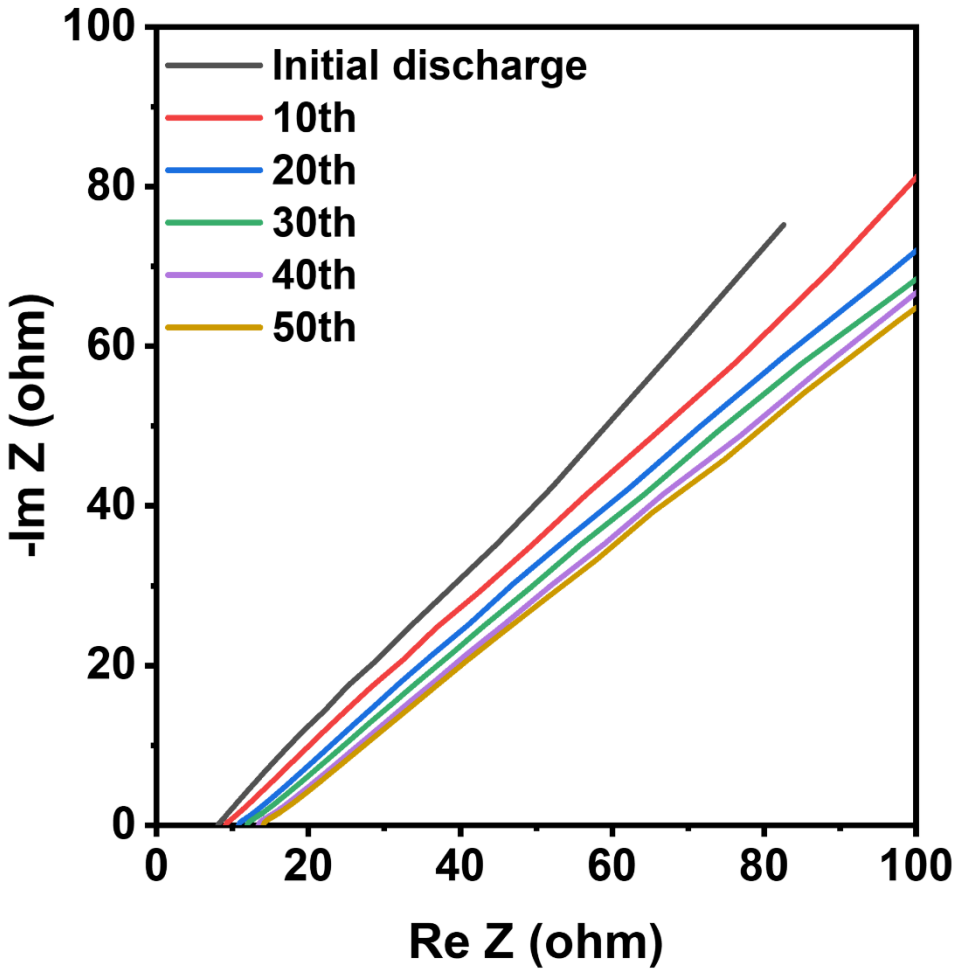

Supplementary Figure 16. The impedance evolution of a CNG/S SSSB over 50 cycles.

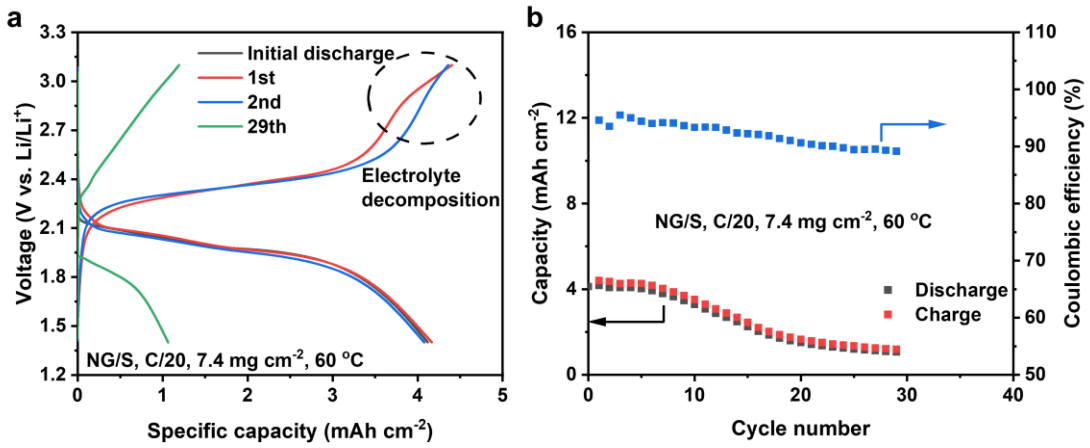

Supplementary Figure 17. Electrochemical performance of Li-In|$LPSCl_{1.5}$|NG/S/$LPSCl_{1.5}$ SSSB at 60 °C. **a**, Voltage profiles at C/20 with a sulfur loading of 7.4 mg cm^{-2}. **b**, Corresponding cycling performance. The electrolyte decomposition can be clearly seen in the charge profile.

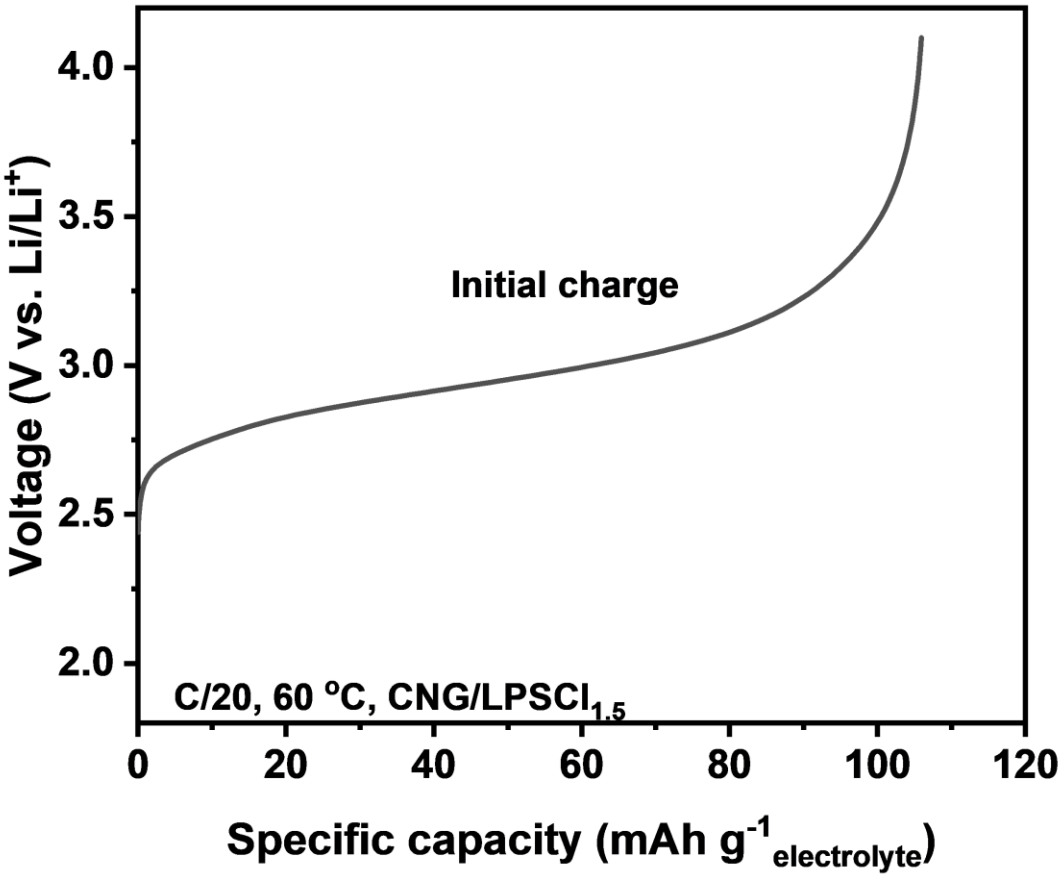

Supplementary Figure 18. Initial charge profile of Li-In|$LPSCl_{1.5}$|CNG/S/$LPSCl_{1.5}$ SSSB at C/20 at 60 °C (S content in CNG/S, 40%).

LIST OF SUPPLEMENTAL TABLES

Supplementary Table 1. DFT calculated surface energies for low Miller index symmetric surface slabs of $LPSC_{1.5}$.

Miller Indices	Surface Composition	Simulated Slab	Surface Energy (J/m^2)
010	S	$Li_{37}P_8S_{35}Cl_{11}$	0.70
010	Li	$Li_{41}P_8S_{35}Cl_{11}$	0.44
010	**Li_5SCl**	**$Li_{36}P_6S_{28}Cl_{10}$**	**0.40**
010	Li_7SCl	$Li_{40}P_6S_{28}Cl_{10}$	0.72
011	Li_4S_2	$Li_{32}P_6S_{26}Cl_{10}$	0.48
011	Li_4S_2	$Li_{34}P_6S_{28}Cl_8$	0.70

Supplementary Table 2. Comparison of our work with recent reported representative SSSBs. Results from our work are shown in bold.

Cathode	Electrolyte	Sulfur content in composite cathode	Sulfur loading (mg cm^{-2})	Anode	N/P ratio	Current density (mA cm^{-2})	Areal capacity (mAh cm^{-2})	Capacity retention, cycles
CNG/S	**$LPSCl_{1.5}$**	**35%**	**3.4**	**Li/In**	**2.22**	**0.577 (C/10)**	**2.62**	**92%, 235**
CNG/S	**$LPSCl_{1.5}$**	**35%**	**6.8**	**Li/In**	**1.21**	**0.570 (C/20)**	**4.94**	**132%, 42**
CNG/S	**$LPSCl_{1.5}$**	**35%**	**7.6**	**Li/In**	**1.21**	**0.639 (C/20, 60 °C)**	**11.3**	**91%, 40**
S/CNF[2]	Li_3PS_4·0.5LiI	35%	2.73	Li	N/A	2.28 (C/2, 60 °C)	2.92	27.4%, 90
S@CNT[3]	LGPS	20.6%	3	$Li_{0.8}Al$	4	0.251 (C/20)	3.46	~81%, 100
S@KB[4]	LGPS	22.5%	6.5	Li/LiI	N/A	0.2 (C/56)	8.87	57.8%, 8
S-CoNC[5]	$Li_7P_3S_{11}$	50%	4	Li/In	4.5	0.2 (C/30)	5.25	88.9%, 100
Mo_6S_8[6]	Li_3PS_4	20%	4.2	Li/In	N/A	3.51 (C/2, 80 °C)	4.87	Only one cycle
S/NWO/CNT[7]	$Li_7P_3S_{11}$	18.5%	8.05	Li/In	N/A	0.674 (C/20)	6.32	~51%, 50
C-FeS_2-S[8]	Li_3PS_4-LiI	15%	2.5	Li	N/A	0.0835 (C/50)	3.55	142%, 7
S-VS_2[9]	Li_3PS_4	20%	5.12	Li/In	N/A	0.12 (C/72)	7.8	66.7%, 10
S-C65[10]	Li_6PS_5Cl	33%	3	$Li_{3.75}Si$	5.12	1.44 (C/3)	2.94	76.3%, 500

S@EG[11]	$Li_{9.54}Si_{1.74}P_{1.44}S_{11.7}Cl_{0.3}$	20%	8.92	Li/In	N/A	0.76 (C/40, 40 ºC)	6	119%, 20
S-KB[12]	Li_3PS_4-$2LiBH_4$	60%	2.57	Li/In	3.58	2.15 (C/2, 60 ºC)	2.58	77.5%, 800
S/CNT/LiI[13]	LGPS	30%	12	Li/In	N/A	0.12 (C/167, 60 ºC)	4.1	65.9%, 50
rGO@S[14]	LGPS	24.6%	0.45	Li	N/A	0.75 (1C, 60 ºC)	0.48	77%, 750
S@BP2000[15]	$Li_7P_3S_{11}$	30%	0.45	Li/In	N/A	2.26 (3C, 80 ºC)	0.55	88.8%, 500
CNTs@S[16]	LGPS	13.2%	0.5	Li	15.5	0.84 (1C, 60 ºC)	0.41	81.2%, 400
S-KB[17]	Li_3PS_4	27%	4.5	Li/In	N/A	0.72 (C/10, 60 ºC)	4.3	92%, 50
S/C[18]	$Li_7P_{2.9}Sb_{0.1}S_{10.75}O_{0.25}$	18%	0.7	Li/In	N/A	0.06 (C/20, 60 ºC)	0.93	91%, 100
S-super P[19]	$Li_7P_3S_{11}$	30%	1.2	Li/In	N/A	1.0 (C/2)	1.25	84.5%, 100
Co@AB/S[20]	Li_6PS_5Cl	40%	4.5	Li/In	N/A	2.2 (C/3, 60 ºC)	5.9	74.1%, 300

References

[1] Schwietert TK, Arszelewska VA, Wang C, Yu C, Vasileiadis A, de Klerk NJJ*, et al.* Clarifying the relationship between redox activity and electrochemical stability in solid electrolytes. *Nat Mater* 2020, **19**(4)**:** 428-435.

[2] Bonnick P, Niitani K, Nose M, Suto K, Arthur TS, Muldoon J. A high performance all solid state lithium sulfur battery with lithium thiophosphate solid electrolyte. *Journal of Materials Chemistry A* 2019, **7**(42)**:** 24173-24179.

[3] Pan H, Zhang M, Cheng Z, Jiang H, Yang J, Wang P*, et al.* Carbon-free and binder-free Li-Al alloy anode enabling an all-solid-state Li-S battery with high energy and stability. *Science Advances*, **8**(15)**:** eabn4372.

[4] Duan C, Cheng Z, Li W, Li F, Liu H, Yang J*, et al.* Realizing the compatibility of a Li metal anode in an all-solid-state Li−S battery by chemical iodine–vapor deposition. *Energy & Environmental Science* 2022, **15**(8)**:** 3236-3245.

[5] Zheng X, Wu Y, Li C, Peng J, Yang W, Lv Z*, et al.* Promoting the conversion of S and Li2S using a Co3O4@NC additive in all-solid-state Li–S batteries. *Journal of Materials Chemistry A* 2022, **10**(36)**:** 18907-18915.

[6] Li M, Pan H, Liu T, Xiong X, Yu X, Hu Y-S*, et al.* All-in-One Ionic–Electronic Dual-Carrier Conducting Framework Thickening All-Solid-State Electrode. *ACS Energy Letters* 2022, **7**(2)**:** 766-772.

[7] Zhao BS, Wang L, Liu S, Li GR, Gao XP. High-Efficiency Hybrid Sulfur Cathode Based on Electroactive Niobium Tungsten Oxide and Conductive Carbon Nanotubes for All-Solid-State Lithium-Sulfur Batteries. *ACS Appl Mater Interfaces* 2022, **14**(1)**:** 1212-1221.

[8] Ulissi U, Ito S, Hosseini SM, Varzi A, Aihara Y, Passerini S. High Capacity All-Solid-State Lithium Batteries Enabled by Pyrite-Sulfur Composites. *Advanced Energy Materials* 2018, **8**(26)**:** 1801462.

[9] Xu S, Kwok CY, Zhou L, Zhang Z, Kochetkov I, Nazar LF. A High Capacity All Solid-State Li-Sulfur Battery Enabled by Conversion-Intercalation Hybrid Cathode Architecture. *Advanced Functional Materials* 2020, **31**(2)**:** 2004239.

[10] Ji W, Zhang X, Liu M, Ding T, Qu H, Qiu D*, et al.* High-performance all-solid-state Li–S batteries enabled by an all-electrochem-active prelithiated Si anode. *Energy Storage Materials* 2022, **53:** 613-620.

[11] Xu G, Yan Z, Yang H, Zhang X, Su Y, Huang Z*, et al.* Multiscale Structural Engineering of Sulfur/Carbon Cathodes Enables High Performance All-Solid-State Li-S Batteries. *Small* 2023, **19**(30)**:** 2300420.

[12] Wang D, Jhang L-J, Kou R, Liao M, Zheng S, Jiang H, *et al.* Realizing high-capacity all-solid-state lithium-sulfur batteries using a low-density inorganic solid-state electrolyte. *Nature*

Communications 2023, **14**(1)**:** 1895.

[13] Kim JT, Rao A, Nie H-Y, Hu Y, Li W, Zhao F, *et al.* Manipulating Li_2S_2/Li_2S mixed discharge products of all-solid-state lithium sulfur batteries for improved cycle life. *Nature Communications* 2023, **14**(1)**:** 6404.

[14] Yao X, Huang N, Han F, Zhang Q, Wan H, Mwizerwa JP, *et al.* High-Performance All-Solid-State Lithium–Sulfur Batteries Enabled by Amorphous Sulfur-Coated Reduced Graphene Oxide Cathodes. *Advanced Energy Materials* 2017, **7**(17)**:** 1602923.

[15] Han Q, Li X, Shi X, Zhang H, Song D, Ding F, *et al.* Outstanding cycle stability and rate capabilities of the all-solid-state Li–S battery with a $Li_7P_3S_{11}$ glass-ceramic electrolyte and a core–shell S@BP2000 nanocomposite. *Journal of Materials Chemistry A* 2019, **7**(8)**:** 3895-3902.

[16] Zhang Q, Huang N, Huang Z, Cai L, Wu J, Yao X. CNTs@S composite as cathode for all-solid-state lithium-sulfur batteries with ultralong cycle life. *Journal of Energy Chemistry* 2020, **40:** 151-155.

[17] Alzahrani AS, Otaki M, Wang D, Gao Y, Arthur TS, Liu S, *et al.* Confining Sulfur in Porous Carbon by Vapor Deposition to Achieve High-Performance Cathode for All-Solid-State Lithium–Sulfur Batteries. *ACS Energy Letters* 2021, **6**(2)**:** 413-418.

[18] Zhao B-S, Wang L, Chen P, Liu S, Li G-R, Xu N, *et al.* Congener Substitution Reinforced $Li_7P_{2.9}Sb_{0.1}S_{10.75}O_{0.25}$ Glass-Ceramic Electrolytes for All-Solid-State Lithium–Sulfur Batteries. *ACS Applied Materials & Interfaces* 2021, **13**(29)**:** 34477-34485.

[19] Zhu X, Jiang W, Zhao S, Huang R, Ling M, Liang C, *et al.* Exploring the concordant solid-state electrolytes for all-solid-state lithium-sulfur batteries. *Nano Energy* 2022, **96:** 107093.

[20] Zhong H, Su Y, Wu Y, Gu J, Ma R, Luo Y, *et al.* Long-Life and High-Loading All-Solid-State Li–S Batteries Enabled by Acetylene Black with Dispersed Co-N_4 as Single Atom Catalyst. *Advanced Energy Materials* 2023, **13**(25)**:** 2300767.